J. Fluid Mech. (2020), *vol.* 889, A10. © The Author(s), 2020.
Published by Cambridge University Press
doi:10.1017/jfm.2020.66

On non-Oberbeck–Boussinesq effects in Rayleigh–Bénard convection of air for large temperature differences

Zhen-Hua Wan[1], Qi Wang[1], Ben Wang[1], Shu-Ning Xia[2], Quan Zhou[2] and De-Jun Sun[1,†]

[1]Department of Modern Mechanics, University of Science and Technology of China, Hefei 230027, PR China

[2]Shanghai Key Laboratory of Mechanics in Energy Engineering, Shanghai Institute of Applied Mathematics and Mechanics, School of Mechanics and Engineering Science, Shanghai University, Shanghai 200072, PR China

(Received 13 July 2019; revised 17 November 2019; accepted 13 January 2020)

We present direct numerical simulations of non-Oberbeck–Boussinesq (NOB) Rayleigh–Bénard (RB) convection due to large temperature differences in two-dimensional (2-D) and three-dimensional (3-D) cells. Perfect air is chosen as the operating fluid and the Prandtl number (Pr) is fixed to 0.71 for the reference state $\hat{T}_0 = 300$ K. In the present system, we consider large temperature differences ranging from 60 K to 240 K, and relatively strong NOB effects are induced at moderate Rayleigh numbers (Ra) in the range $3 \times 10^6 \leqslant Ra \leqslant 5 \times 10^9$. The large temperature difference also induces the turbulence system with large density variation. Due to top-down symmetry breaking under NOB conditions, an increase of the centre temperature T_c is found compared to the arithmetic mean temperature T_m of the top and bottom plates, and the shift of T_c is strongly dependent on Rayleigh number Ra and temperature differential ϵ. The NOB effects on the Nusselt number (Nu) are quite small ($\lesssim 2\,\%$). The power-law scalings of Nu versus Ra are robust against NOB effects, even for the extremely large temperature difference 240 K, which has never been reached in previous experiments and simulations. The Reynolds numbers Re, as well as the scalings of Re versus Ra, are also insensitive to NOB effects. It is noteworthy that the influence of NOB effects on Nu and Re in 3-D RB flow are weaker than its 2-D counterpart. Furthermore, the extended laminar boundary layer (BL) equations are developed based on the low-Mach-number Navier–Stokes equations, which qualitatively predicts the NOB effects on velocity profiles. Direct numerical simulation results indicate that the top and bottom thermal BLs can compensate each other much better than the velocity BLs under NOB conditions, which contribute to the robustness of Nu.

Key words: Bénard convection, convection in cavities

†Email address for correspondence: dsun@ustc.edu.cn

1. Introduction

Turbulent Rayleigh–Bénard (RB) convection by now has been studied extensively, in which the fluid is heated from below and cooled from above (see, e.g. Bodenschatz, Pesch & Ahlers (2000), Ahlers, Grossmann & Lohse (2009), Lohse & Xia (2010), Chillà & Schumacher (2012), Xia (2013)). Most of these studies strive to stay in a limit described by the Oberbeck–Boussinesq (OB) approximation, which relies on satisfying the following main assumptions: the density is regarded a constant except in the buoyancy term, where the density ρ is assumed to be linearly dependent on temperature T; all fluid properties (e.g. thermal conductivity k, dynamic viscosity μ) are considered constants.

The OB approximation is found to be reasonably satisfactory if the temperature difference is below a certain threshold which is different for different fluids (Gray & Giorgini 1976). However, large temperature differences are ubiquitous in many practical applications, where non-Oberbeck–Boussinesq (NOB) effects become significant. For instance, in nuclear reactors where the typical temperature differences of thermal insulation systems can reach up to several hundred degrees, the variations of ρ, k and μ must be taken into account simultaneously. In foundry processes and some astrophysical flows, NOB effects also play an important role.

There is by now a large body of literature on NOB effects in RB convection (Ahlers *et al.* 2009; Chillà & Schumacher 2012) for various fluids, such as gaseous helium (Wu & Libchaber 1991; Sameen, Verzicco & Sreenivasan 2008), glycerol (Zhang, Childress & Libchaber 1997, 1998; Sugiyama *et al.* 2007; Horn, Shishkina & Wagner 2013), gaseous ethane (Ahlers *et al.* 2007, 2008), water (Ahlers *et al.* 2006; Sugiyama *et al.* 2009; Horn & Shishkina 2014; Demou & Grigoriadis 2019), SF_6 (Burnishev, Segre & Steinberg 2010; Burnishev & Steinberg 2012) and air (Xia *et al.* 2016; Liu *et al.* 2018). In general, NOB effects in turbulent RB convection can be induced by two paths (Chillà & Schumacher 2012). One is related to the convection beyond the incompressible limit, which mainly occurs in gases (Ahlers *et al.* 2007), in which the strong compressibility effects and large variations of the fluid properties can arise. The other is usually found in liquids, where NOB effects are almost induced solely from the temperature-dependent material properties (Ahlers *et al.* 2006). In early experiments of Zhang *et al.* (1997), an important issue relevant for NOB effects in RB convection was confirmed, that is, that the flow structures become asymmetric due to a top-down symmetry breaking. With the asymmetry of top and bottom thermal boundary layers (BLs), the temperature at the cell centre will deviate from the arithmetic average of the temperatures at the top and bottom plates. For the convection in water, Ahlers *et al.* (2006) experimentally found that the Nusselt number Nu and Reynolds number Re are rather insensitive to the NOB effects, which only result in a small reduction of Nu ($\lesssim 2\%$) under NOB conditions. No obvious modification of Re is found within the experimental resolution. The centre temperature is increased due to NOB effects. While for gaseous ethane, Ahlers *et al.* (2007) found a decrease of the centre temperature and an increase of Nu which are of opposite and greater magnitude than those for NOB effects in water. Direct numerical simulations (DNS) were performed by Sameen, Verzicco & Sreenivasan (2009) to disentangle the importance of different material parameters for the NOB effects on heat transport and flow structures. More recently, Valori *et al.* (2017) performed an experimental study of the whole velocity field under NOB conditions. The prior studies indicated the fact that NOB effects depend very sensitively on the particular working fluid. The NOB effects are especially relevant to high-Ra convection where

the temperature difference is usually large; however, the NOB effects in various fluids at high *Ra* are still poorly understood (Chillà & Schumacher 2012).

In RB convection of air with large temperature differences, the flow reversals (Xia *et al.* 2016) and instabilities (Liu *et al.* 2018) have recently been studied; however, the heat and momentum transports for relatively high *Ra* have rarely been studied. In order to fill this gap, we investigate NOB effects for compressible air via DNS in two-dimensional (2-D) and three-dimensional (3-D) cells. To induce NOB effects, we consider large temperature differences ranging from 60 K to 240 K. With large variations in fluid properties, especially the large density variations, we try to understand such NOB effects on heat and momentum transport as well as flow structures quantitatively. There are three major purposes for choosing this model. Firstly, we can study strong NOB effects on heat transport induced by large temperature differences in a moderate range of Rayleigh numbers. Secondly, the relationships between fluid properties and temperature are well described by Sutherland's law, which permits us to investigate the influences of variations in μ and k in an accurate way. Finally, flow compressibility with a rather large density variation is appropriately taken into account by employing low-Mach-number Navier–Stokes equations with acoustic waves filtered (Paolucci 1982). In short, this study is favourable for inferring the possible influence of large temperature differences and fluid compressibility on heat transport and flow structures in some high *Ra* experiments that usually encounter large temperature differences. To the best of our knowledge, the extremely large temperature difference (e.g. $\Delta\hat{T} = 240$ K) has never been reached in previous experiments and simulations, which is several times that of the largest one used in previous studies. In addition, the low-Mach-number Navier–Stokes equations are also firstly employed to treat 3-D fully turbulent convection at relatively high *Ra* with large density variations (Livescu 2020).

The reminder of this paper is organized as follows. In § 2 we describe the detailed numerical procedures. In § 3 we show the major results for the OB and NOB cases, including the flow organizations, heat and momentum transport, and BL profiles, etc. In § 4 we summarize our findings and conclude the paper.

2. Numerical procedures

In figure 1 we show the configuration of the present system in which the working fluid is air in a cell of width $\hat{W}$, height $\hat{H}$ and depth $\hat{D}$ (for 3-D cases), where '$\hat{\cdot}$' denotes dimensional quantities. Height $\hat{H}$ is chosen as the reference length. For all cases, $\hat{D}/\hat{W} = 1$ and $\hat{W}/\hat{H} = 1$. The bottom and top walls are fixed at temperatures of $\hat{T}_H$ and $\hat{T}_C$, with $\hat{T}_H > \hat{T}_C$, while the lateral walls are thermally insulated. No-slip and non-penetrative boundary conditions are applied at all rigid walls. To treat NOB effects in air due to a large temperature difference, we employ low-Mach-number Navier–Stokes equations (Paolucci 1982). The reference temperature $\hat{T}_0 = (\hat{T}_H + \hat{T}_C)/2$ is chosen to be 300 K, and the reference quantities such as $\hat{\mu}_0, \hat{k}_0, \hat{c}_{p0}$ are determined at this temperature (Xia *et al.* 2016). The dimensional temperature difference is $\Delta\hat{T} = \hat{T}_H - \hat{T}_C = 2\epsilon\hat{T}_0$, where ϵ is the temperature differential, quantifying the intensity of NOB effects, with $\epsilon \leqslant 0.4$ corresponding to $\Delta\hat{T} \leqslant 240$ K. The dimensionless temperatures T at the hot and cold walls are given by $1+\epsilon$ and $1-\epsilon$, respectively. The free-fall velocity $\hat{u}_0 = (2\epsilon\hat{g}\hat{H})^{1/2}$ is used as the reference velocity, where $\hat{g}$ is the gravitational acceleration, and, thus, the reference time is $\hat{t}_0 = \hat{H}/\hat{u}_0$. The hydrodynamic pressure π is non-dimensionalized by $\hat{\rho}_0\hat{U}^2$, and the thermodynamic

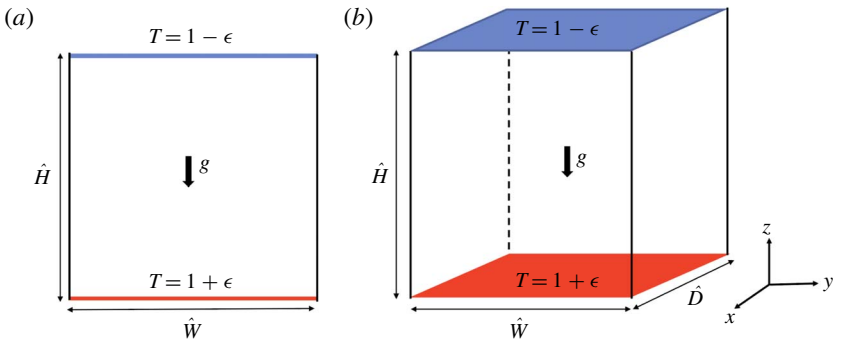

FIGURE 1. Sketch of the present Rayleigh–Bénard convection in (*a*) 2-D and (*b*) 3-D cells with the working fluid air, where $\hat{D}/\hat{W}=1$ and $\hat{W}/\hat{H}=1$.

pressure p is non-dimensionalized by $\hat{\rho}_0\hat{R}\hat{T}_0$, where $\hat{R}$ is the gas constant. Finally, the dimensionless form of low-Mach-number Navier–Stokes equations with acoustic waves filtered can be written as

$$\frac{\partial \rho}{\partial t}+\frac{\partial \rho u_j}{\partial x_j}=0, \tag{2.1}$$

$$\frac{\partial \rho u_i}{\partial t}+\frac{\partial \rho u_i u_j}{\partial x_j}=-\frac{\partial \pi}{\partial x_j}+\sqrt{\frac{Pr}{Ra}}\frac{\partial \tau_{ij}}{\partial x_j}+\frac{1}{2\epsilon}(\rho-1)\boldsymbol{n}_i, \tag{2.2}$$

$$\rho c_p\left(\frac{\partial T}{\partial t}+u_j\frac{\partial T}{\partial x_j}\right)=\frac{1}{\sqrt{RaPr}}\frac{\partial}{\partial x_j}k\frac{\partial T}{\partial x_j}+\Gamma\frac{\mathrm{d}p}{\mathrm{d}t}, \tag{2.3}$$

$$p=\rho T, \tag{2.4}$$

where $\boldsymbol{n}_i$ is the unit vector in the direction of gravity and k is the thermal conductivity. The ratio of the specific heats is $\gamma=1.4$. Denote by $\Gamma=(\gamma-1)/\gamma$ the measure of the resilience of the fluid. The isobaric specific heat c_p is fixed to 1. Let π be the hydrodynamic pressure. Let p be the thermostatic pressure; for a more detailed definition, see Xia *et al.* (2016) and Liu *et al.* (2018). The viscous stress tensor τ_{ij} is expressed as $\tau_{ij}=\mu(\partial u_i/\partial x_j+\partial u_j/\partial x_i)-(2/3)\delta_{ij}\mu\partial u_k/\partial x_k$, where δ_{ij} is the Kronecker delta function. The four control dimensionless parameters of this problem are the temperature differential ϵ, Rayleigh number Ra, Prandtl number Pr and aspect ratio A, defined as

$$\epsilon\equiv\frac{\Delta\hat{T}}{2\hat{T}_0},\quad Ra\equiv\frac{2\epsilon\hat{c}_{p0}\hat{\rho}_0^2\hat{g}\hat{H}^3}{\hat{\mu}_0\hat{k}_0},\quad Pr\equiv\frac{\hat{c}_{p0}\hat{\mu}_0}{\hat{k}_0},\quad A\equiv\frac{\hat{W}}{\hat{H}}. \tag{2.5a–d}$$

We fixed the reference Pr to 0.71 and A to 1. Dimensionless thermal conductivity k and dynamic viscosity μ are determined by Sutherland's law:

$$k=T^{1.5}(1+S_k)/(T+S_k),\quad \mu=T^{1.5}(1+S_\mu)/(T+S_\mu). \tag{2.6a,b}$$

For air, the dimensionless Sutherland constants $S_k=\hat{S}_k/\hat{T}_0=0.648$ and $S_\mu=\hat{S}_\mu/\hat{T}_0=0.368$ for the reference state $\hat{T}_0=300$ K (White 1974; Suslov & Paolucci 1999; Suslov 2010). Sutherland's law is developed based on the kinetic theory of ideal gases and an

idealized intermolecular-force potential (Sutherland 1893), which is commonly used in fully compressible flows (Chen, Xu & Lu 2010; Pirozzoli, Bernardini & Grasso 2010; Wan *et al.* 2013). Fairly accurate results can be obtained with an error less than a few per cent over a wide range of temperatures. Oberbeck–Boussinesq cases are also investigated for the purpose of making a comparison. We set $\epsilon = 0.005$, $\mu = k = p = 1$, $\partial u_j/\partial x_j = 0$ and $\rho = 1$ except in the buoyancy term $\rho = 1/T = 1/(1+\delta T) \approx 1 - \delta T$, so the equations (2.1)–(2.4) can be reduced to the classical OB equations (van der Poel *et al.* 2015; Wang *et al.* 2018).

The governing equations are solved numerically by our in-house code *lMn2d/3d*. In this solver, all spatial terms are discretized by a second-order central difference scheme. To avoid pressure–velocity decoupling, the staggered grid is utilized for temperature and velocities, and pressure is also staggered in time with all other variables. The fractional-step method is used to solve the equations (Verzicco & Orlandi 1996). A multi-grid strategy (Briggs, Henson & McCormick 2000) is adopted to solve the pressure Poisson equation. For time advancement, the wall-normal viscous terms are semi-implicitly treated with the Crank–Nicolson scheme, while all other terms are discretized by the third-order Runge–Kutta scheme. The numerical details and validations of the code have been elaborated on in our previous works (Xia *et al.* 2016; Liu *et al.* 2018; Wang *et al.* 2019*a*). The grid sizes and some other simulation parameters are given in tables 3 and 4 in the Appendix. For all simulations, the *Nu* and *Re* are averaged for at least 400 free-fall time units after all transients have been dissipated. The grid is chosen to satisfy the resolution requirement which can resolve the smallest scales of the problem, i.e. the Kolmogorov scale η_K and the Batchelor scale η_B (Shishkina *et al.* 2010). In addition, a non-uniform grid is adopted with more grid points clustered near walls in order to resolve small scales inside BLs. For all cases, there are at least 10 grid points inside the thermal BLs.

3. Results and discussion

3.1. *Flow organization*

3.1.1. *The velocity fields*

In figure 2(*a–d*) we show the instantaneous velocity and reduced temperature fields at $Ra = 5 \times 10^8$ and 8×10^8 for OB and $\epsilon = 0.2$. Here, the reduced temperature is defined as

$$\Theta = (T - 1)/2\epsilon. \tag{3.1}$$

In 2-D simulations the velocity fields are very complex, even when we miss 3-D flow modes. As shown in figure 2(*a*,*b*), we can find a relatively stable large-scale circulation (LSC) at $Ra = 5 \times 10^8$, the size of which is comparable to the box size H in both OB and NOB cases (Xi, Lam & Xia 2004; Sugiyama *et al.* 2009; Chandra & Verma 2013). As *Ra* increases, the instantaneous velocity fields that the corner rolls become more unstable and the relatively stable LSC is broken. For the case $Ra = 8 \times 10^8$ shown in figure 2(*c*,*d*), some relatively large-scale vortices detach from the corners and convect along the main wind. Movies at different *Ra* are provided in the supplementary materials available at https://doi.org/10.1017/jfm.2020.66. It should be mentioned that the LSC can still be observed from the mean flow field in this case, but the mean velocity distribution is changed, which will be further discussed in the following. In figure 2(*e*,*f*) we show the volume rendering of 3-D temperature fields. Vigorous sheetlike plumes are emitted from the bottom and top plates, with no significant differences in plume structures between the OB and NOB cases. Overall,

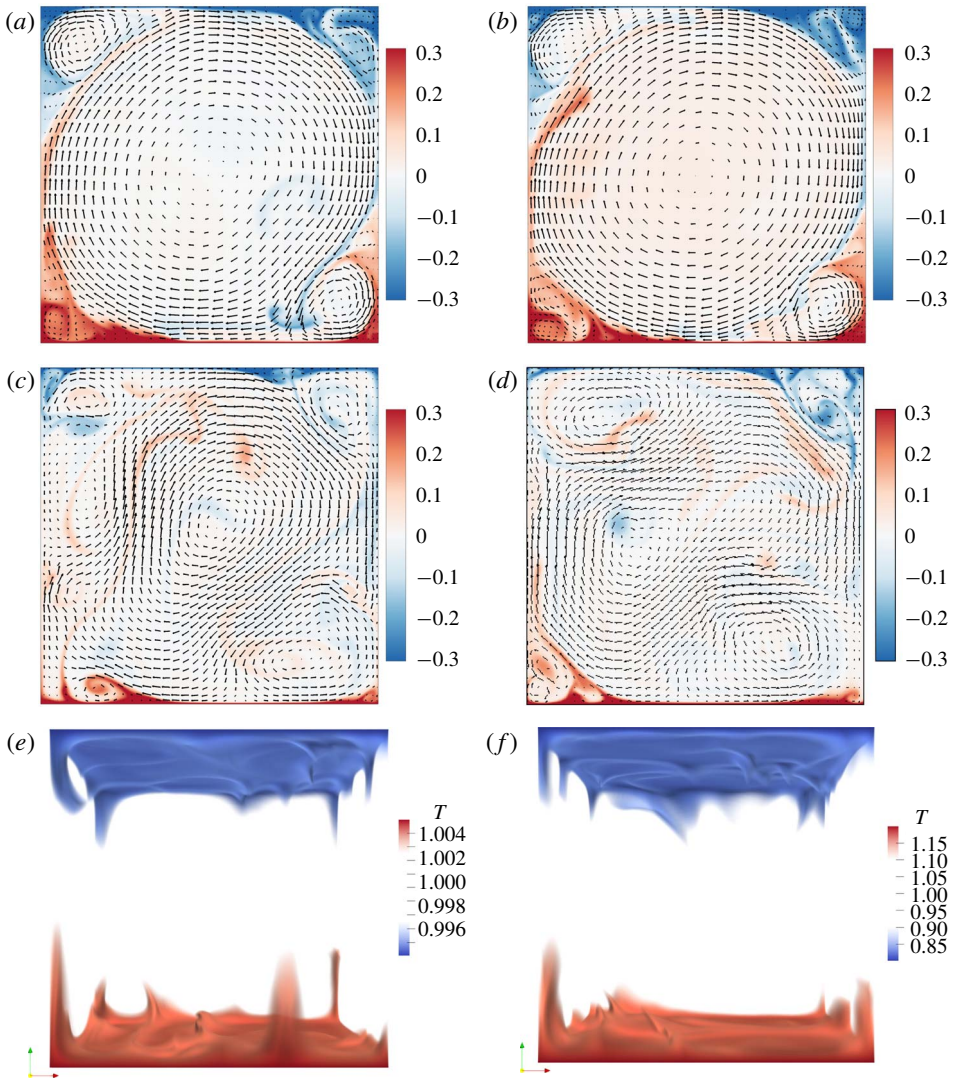

FIGURE 2. Snapshots of the 2-D velocity (arrows) and reduced temperature Θ (colour) fields for $Pr = 0.71$ with different ϵ and Ra. (*a,b*) $Ra = 5 \times 10^8$; (*a*) OB, (*b*) $\epsilon = 0.2$. (*c,d*) $Ra = 8 \times 10^8$; (*c*) OB, (*d*) $\epsilon = 0.2$. (*e,f*) Volume rendering of 3-D temperature fields (T) for $Ra = 10^7$; (*e*) OB, (*f*) $\epsilon = 0.2$.

for air, we cannot observe obvious qualitative differences from the snapshots between OB and NOB cases for the same Ra, which is different from the NOB cases in water (Sugiyama *et al.* 2009).

To better show NOB effects on the velocity field, we present in figure 3 the mean horizontal velocity profiles $\bar{v}(z)$ at $y = 0.5$ and mean vertical velocity profiles $\bar{w}(y)$ at $z = 0.5$ for $Ra = 10^8$ and 10^9 in OB and various ϵ in 2-D cases, respectively. Due to the inherent nature of top-down symmetry breaking, the flow structures will be asymmetric as stated in (Zhang *et al.* 1997). From figure 3, we can see that the profiles of the horizontal velocity $\bar{v}(z)$ and the vertical velocity $\bar{w}(y)$ become asymmetric to a certain degree. It should be mentioned that the profiles at $Ra = 10^9$

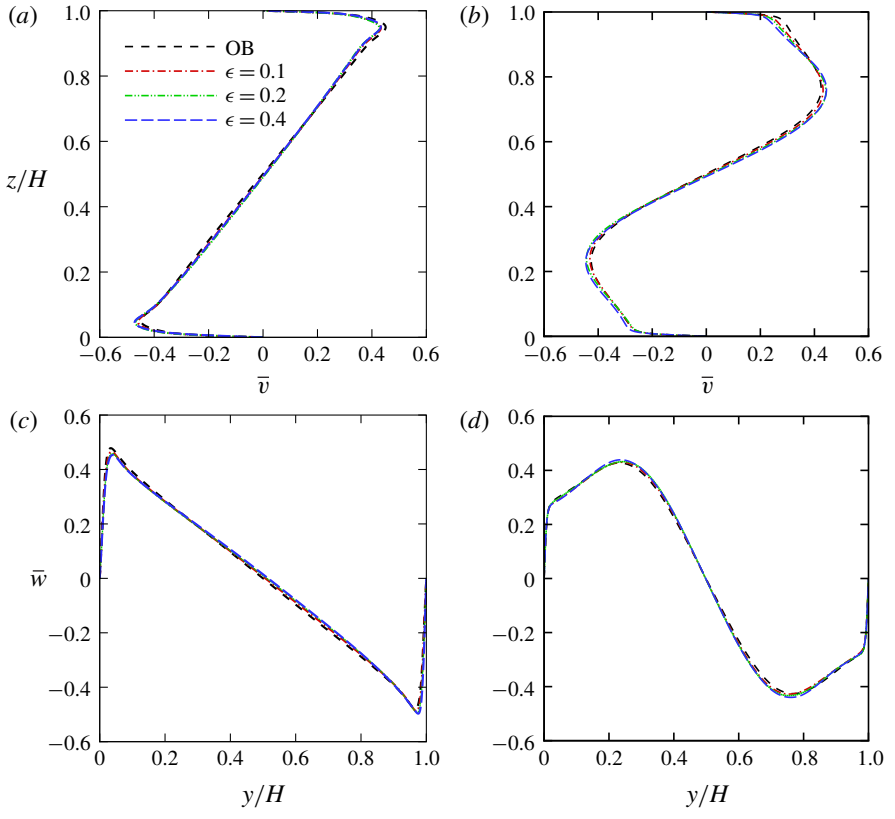

FIGURE 3. Mean velocity profiles of $\bar{v}(z)$ for 2-D cases in the plane of $y = 0.5$ (*a*,*b*) and $\bar{w}(y)$ in the plane of $z = 0.5$ (*c*,*d*) for (*a*,*c*) $Ra = 10^8$ and (*b*,*d*) $Ra = 10^9$.

shown in figure 3(*b*) are different from those at $Ra = 10^8$ shown in figure 3(*a*), due to the change of flow pattern as illustrated in figure 2. At $Ra = 10^8$, there is a relatively stable LSC, giving rise to the peaks of the profile near the edge of the top/bottom viscous BL. However, at $Ra = 10^9$, the stable LSC is broken and there are large vortices detached from corner rolls, and the convection of those large vortices has led the peaks of the profile occurring in the bulk (e.g. $z \simeq 0.2$ at the bottom) rather than the edge of the viscous BL. Interestingly, even without stable LSC in this case, we can still find the BL structures and a relatively sharp transition of the velocity profiles occurring near the edge of the viscous BL. In § 3.4 we will further discuss the NOB effects on the profiles of the viscous BLs, which can be described qualitatively by laminar BL theory.

In order to quantify the intensity of velocity asymmetry, for 2-D cases, the absolute value of the ratio of horizontal maximum mean velocity $\bar{v}_{max}$ and horizontal minimum mean velocity $\bar{u}_{min}$ is calculated, namely, $\bar{v}_r = |\bar{v}_{max}|/|\bar{v}_{min}|$, and a similar ratio is also obtained for the vertical velocity $\bar{w}_r = |\bar{w}_{max}|/|\bar{w}_{min}|$. In figure 4 we show $\bar{v}_r$ and $\bar{w}_r$ as a function of Ra for different ϵ. It is well known that the velocity ratios should be equal to 1 within OB approximation due to inherent symmetry of the system, while they deviate from 1 under NOB conditions. Here, we can see that $\bar{v}_r$ or $\bar{w}_r$ is a non-monotonic function of Ra for different ϵ. For $Ra \lesssim 8 \times 10^8$, $\bar{v}_r$ shows a strong deviation under NOB conditions, and the maximum deviation is around 8 % at

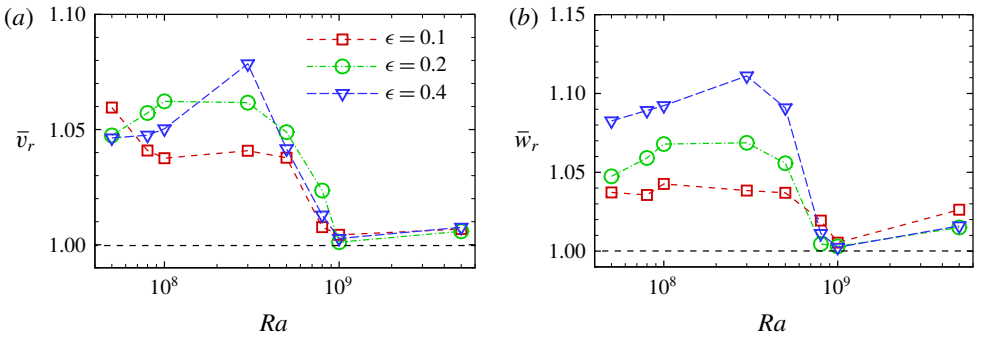

FIGURE 4. Graphs of $\bar{v}_r$ (*a*) and $\bar{w}_r$ (*b*) versus Ra for different ϵ for 2-D cases.

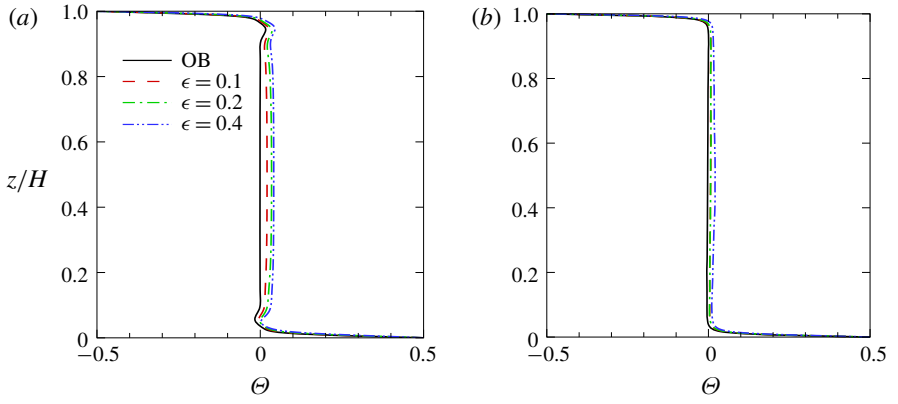

FIGURE 5. The profiles of time-averaged reduced temperatures $\langle\Theta\rangle_t$ for 2-D cases at $y = 0.5$ for (*a*) $Ra = 10^8$ and (*b*) $Ra = 10^9$.

$Ra = 3 \times 10^8$ with $\epsilon = 0.4$. Similar behaviors are found for $\bar{w}_r$. Furthermore, the most interesting feature is that the Ra dependence of $\bar{v}_r$ or $\bar{w}_r$ is not monotonous, similar to the convection of air with NOB effects in a differentially heated cell (Wang *et al.* 2019*a*). Based on the present data, it seems that the asymmetric feature of velocity is weakened for high Ra, which should also be attributed to the change of flow pattern when $Ra \gtrsim 8 \times 10^8$, as illustrated in figure 2.

3.1.2. *The temperature profiles and shift of centre temperature*

Apart from the velocity distribution, the NOB effects also exert a significant influence on the temperature field. Here, we are committed to studying the influence of NOB effects on temperature profiles and centre temperature quantitatively. Within OB approximation, the centre temperature T_c should be equal to 1 (or $\Theta_c = 0$). However, the T_c measured under NOB conditions will deviate from this mean value, due to the asymmetry between top and bottom thermal BLs (Ahlers *et al.* 2007; Sugiyama *et al.* 2009; Horn *et al.* 2013; Weiss *et al.* 2018). For instance, with much smaller μ/k, the thicknesses of viscous/thermal BLs near the cold wall become much thinner in the present system (Xia *et al.* 2016).

In figure 5 we show the profiles of time-averaged reduced temperatures $\langle\Theta\rangle_t$ on the line at $y = 0.5$ in 2-D OB and NOB cases with different ϵ and Ra. For OB cases, Θ in

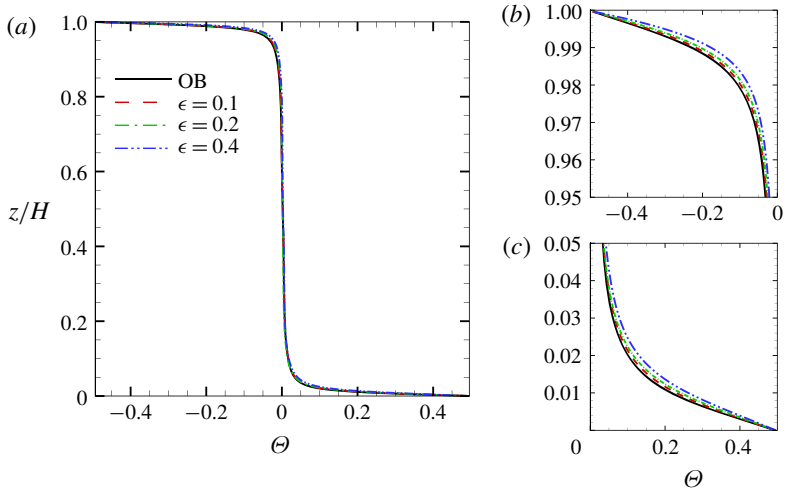

FIGURE 6. (*a*) The profiles of time- and plane-averaged reduced temperatures $\langle\Theta\rangle_{t,S}$ for a 3-D case at $Ra = 10^8$. Panels (*b*) and (*c*) are the local enlargement of (*a*).

the bulk is nearly zero, and slight overshoots are observed near the edge of the thermal BL for $Ra = 10^8$, which is influenced by the relatively large size corner rolls. Such overshoots can also be observed in NOB cases. At $Ra = 10^9$, the overshoots disappear since these corner rolls are smaller and detach from the corner frequently. For NOB cases, Θ in the bulk become positive for various ϵ and Ra. This finding is similar to that in strongly turbulent RB convection in liquids (Ahlers *et al.* 2006), which is opposed to the previous finding for ethane gas close to its critical point (Ahlers *et al.* 2007). It should be mentioned that the prediction of the central temperature is still a tough task because of the nonlinear temperature dependence of material properties. In the present system, the thermal conductivity increases with the increase in temperature, similar to that in liquids instead of gaseous ethane close to its critical point, which might play a dominant role. In figure 6 we show the profiles of time- and plane-averaged reduced temperatures $\langle\Theta\rangle_{t,S}$ for the 3-D case at $Ra = 10^8$ for various ϵ. The asymmetry of top and bottom thermal BLs is still presented under NOB conditions, but the shift of T_c in the bulk becomes much smaller. At $z/H = 0.5$, the centre reduced temperature Θ_c is of the order 10^{-3}, which is almost close to the level of statistical uncertainties. The NOB effects on the shift of T_c are greatly reduced in 3-D cases, which has not been fully understood. We guess that it might be attributed to better fluid mixing for air in the bulk with the flow motion in the third dimension.

In the present cases, we conjecture that the positive shift of T_c is mainly attributed to the temperature-dependent thermal conductivity k. In other word, the sign of Θ_c can be judged beforehand based on the solution of the motionless state as follows. It is well known that the motionless conductive state is always a solution of the system before convection onset, which can be used as the base flow for studying onset of instability (Liu *et al.* 2018). With fixed temperatures at the top and bottom boundaries, the profiles of temperature T for different ϵ can be obtained by solving the nonlinear

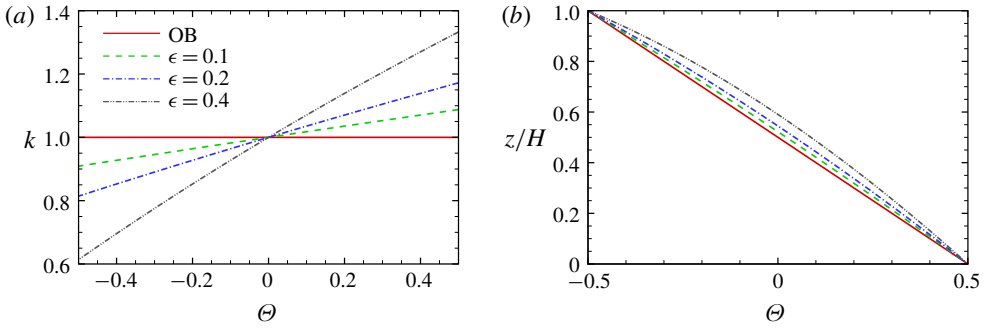

FIGURE 7. (*a*) Variations of k with Θ. (*b*) The profiles of Θ for OB and various ϵ cases at the motionless state.

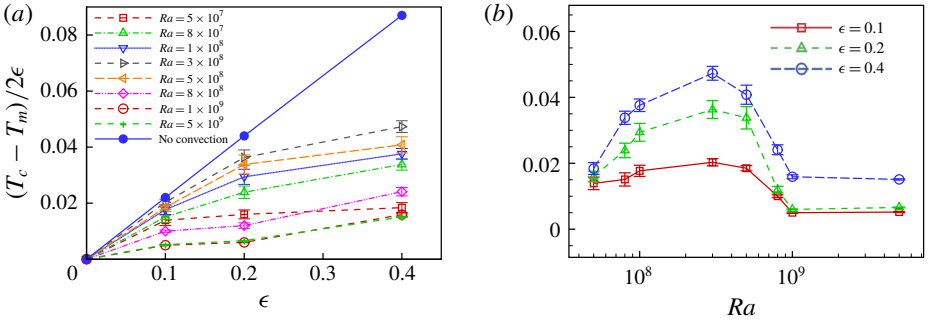

FIGURE 8. (*a*) The relative deviations versus ϵ for air for various Ra in 2-D cases. (*b*) The relative deviations as a function of Ra for various ϵ in 2-D cases.

equation

$$\frac{\mathrm{d}}{\mathrm{d}z}\left(k\frac{\mathrm{d}T}{\mathrm{d}z}\right) = 0, \tag{3.2}$$

with given boundary conditions at the top and bottom plates

$$T|_{z=H} = 1 - \epsilon, \quad T|_{z=0} = 1 + \epsilon.$$

In figure 7(*a*) we show the thermal conductivity k as a function of Θ, while the profiles of temperature in the conduction state in the OB and NOB cases are presented in figure 7(*b*). It is seen that T_c will always be higher than 1 in the present cases, which is qualitatively in consistence with the present DNS results shown in figure 5. The shifts of T_c at the cell centre under motionless states are around 0.022, 0.044 and 0.087 for $\epsilon = 0.1, 0.2$ and 0.4, respectively, which will be compared with DNS results with turbulent convection at relatively high Ra.

As mentioned before, the shift of T_c is greatly reduced in 3-D cases; thus, in figure 8(*a*) we only show the relative deviation $(T_c - T_m)/2\epsilon$ at the cell centre versus ϵ at various Ra in 2-D cases. We can see that all deviations are positive, in qualitative agreement with predictions under motionless states as shown in figure 7.

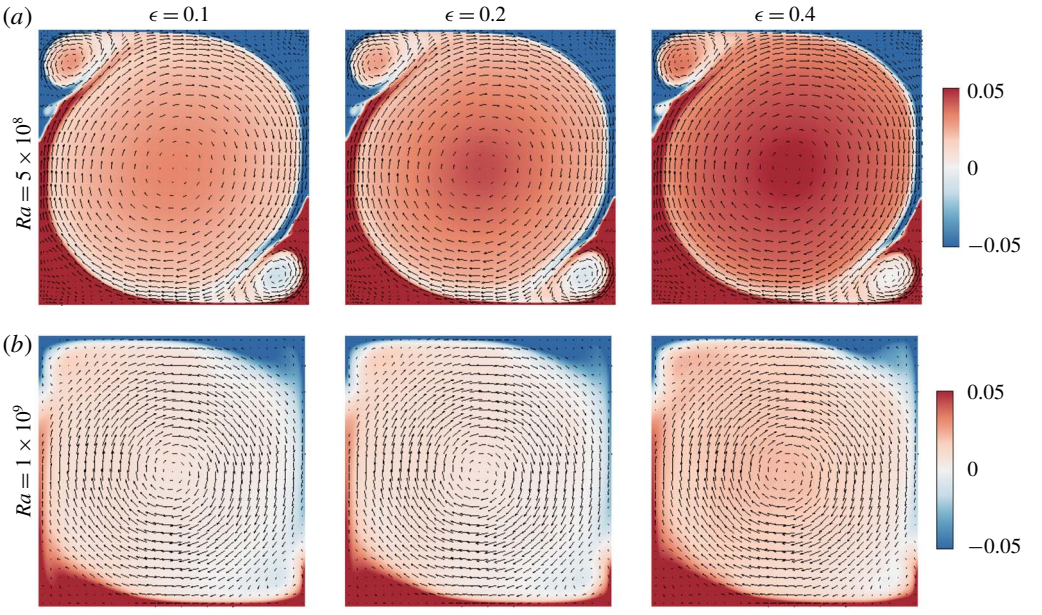

FIGURE 9. The time-averaged temperature $(T - T_m)/2\epsilon$ fields at (*a*) $Ra = 5 \times 10^8$ and (*b*) $Ra = 10^9$ under NOB conditions. The mean velocity vectors are also shown.

This is similar to the finding for water (Sugiyama *et al.* 2009). Moreover, the T_c is strongly dependent on Ra, and the maximum relative deviation is about 5 %, occurring at $Ra = 3 \times 10^8$, but all the relative deviations are below the values of the motionless states. Previously, for convection in water under NOB conditions, Sugiyama *et al.* (2009) found that the relative deviation is rather independent of Ra as $Ra \gtrsim 10^5$ and it almost increases linearly with increasing temperature difference. However, for 2-D RB convection of air with a large temperature difference, the data points of relative deviations are quite scattered, and such a linear relationship seems to be no longer valid. Furthermore, for RB convection in water with NOB effects, the T_c can even be reasonably predicted by the extended Prandtl–Blasius BL theory (Ahlers *et al.* 2006) despite the large deviations in the temperature profiles. Nevertheless, due to the strong scatter and Ra dependence of our data, we cannot directly borrow the extended BL theory to predict T_c in the present cases. In figure 8(*b*) we show relative deviations versus ϵ for different Ra. Clearly, the largest deviations occur at $\epsilon = 0.4$ for all Ra numbers. Similar to $\bar{v}_r$ or $\bar{w}_r$, the Ra dependence of T_c is not monotonous. Interestingly, for $Ra \gtrsim 5 \times 10^8$, the value of relative deviation will not be enhanced, but reduced slightly for all ϵ as Ra increases, which might be attributed to the altered flow organizations. In figure 9 we show the mean temperature fields $(T - T_m)/2\epsilon$ at $Ra = 5 \times 10^8$ and 10^9. It is clear that the size of the corner roll is smaller at $Ra = 10^9$ than at $Ra = 5 \times 10^8$, and the former case has a smaller value of $(T_c - T_m)/2\epsilon$. The mean flow organization at $Ra = 10^9$ for the $\epsilon = 0.1$ case is quite similar to that for the $\epsilon = 0.2$ case, and then we can see that their values of $(T_c - T_m)/2\epsilon$ are very close, as shown in figure 8(*b*). The $\epsilon = 0.4$ case at $Ra = 10^9$ has a larger hot left-bottom

Case	OB	$\epsilon = 0.1$	$\epsilon = 0.2$	$\epsilon = 0.4$
2-D	$Nu \simeq 0.109Ra^{0.295}$	$Nu \simeq 0.110Ra^{0.295}$	$Nu \simeq 0.116Ra^{0.292}$	$Nu \simeq 0.107Ra^{0.296}$
3-D	$Nu \simeq 0.164Ra^{0.285}$	$Nu \simeq 0.169Ra^{0.283}$	$Nu \simeq 0.167Ra^{0.284}$	$Nu \simeq 0.168Ra^{0.282}$

TABLE 1. The best power-law fit of $Nu \sim Ra^{\alpha}$ for OB and various ϵ cases in 2-D and 3-D cases.

corner roll, which produces a larger relative deviation at the cell centre. Thus, except for the boundary layers, we think the flow organization also plays a certain role in determining the relative deviation at the cell centre.

3.2. *Global heat transport*

We now pay attention to the global heat transport with and without NOB effects, which is measured by the Nusselt number Nu, defined as

$$Nu = \frac{Q}{k2\epsilon/H}, \tag{3.3}$$

where Q is the heat flux across any horizontal plane. In figures 10(*a*) and 10(*c*) we show the log–log plot of Nu versus Ra for OB and NOB cases for various ϵ. It is clear that the change of Nu caused by NOB effects is quite small, which cannot be distinguished directly in a log–log plot. Therefore, we list the raw data of Nu for all cases in tables 3 and 4. It is well known that in RB convection for a fixed Pr, the relationship between Nu and Ra can usually be expressed by a power-law scaling, i.e. $Nu \sim Ra^{\alpha}$. For 2-D RB convection within OB approximation, Zhang, Zhou & Sun (2017) examined Ra scalings of Nu for $Pr = 0.7$ and $Pr = 5.3$, which yielded $Nu \sim Ra^{0.30\pm0.02}$ for both Pr. Presently, in table 1 we list the best power-law fitting to Nu versus Ra for OB and various ϵ cases. Clearly, for current 2-D cases in the Ra number range $5 \times 10^7 \leqslant Ra \leqslant 5 \times 10^9$, the Nu versus Ra for OB cases yields $Nu \sim Ra^{0.295}$, which is very close to that in (Johnston & Doering 2009; van der Poel *et al.* 2012; Zhang *et al.* 2017; Wang *et al.* 2019*b*). It should be emphasized that the Ra-scaling exponents are also insensitive to NOB effects in RB convection despite the changes in flow organizations caused by top-down symmetry breaking, similar to the differentially heated cavity (Wang *et al.* 2019*a*). For present 3-D cases in the Ra number range $3 \times 10^6 \leqslant Ra \leqslant 10^8$, the Nu versus Ra for OB cases yields $Nu \sim Ra^{0.285}$, which is also close to its 2-D counterpart.

In addition, to quantitatively show the NOB effects on Nu, the Nusselt number ratio Nu_{NOB}/Nu_{OB} versus ϵ for all Ra is shown in figures 10(*b*,*d*). As previously mentioned, the flow organizations are changed due to NOB effects, including the mean velocity and temperature profiles. However, the Nusselt number Nu seems to be insensitive to changes in ϵ, even up to $\epsilon = 0.4$, corresponding to the dimensional temperature difference 240 K. For 2-D cases, the maximum deviation of Nu_{NOB}/Nu_{OB} from 1 for all Ra is less than 2 %. It is also found that the maximum deviation for 3-D cases ($\lesssim$1 %) is even smaller than that for 2-D cases. Interestingly, similar to Ra dependence of T_c, the Nusselt number ratios display an obvious dependence on Ra in spite of the limited deviations, while they are only weakly dependent on Ra for water with NOB effects (Sugiyama *et al.* 2009).

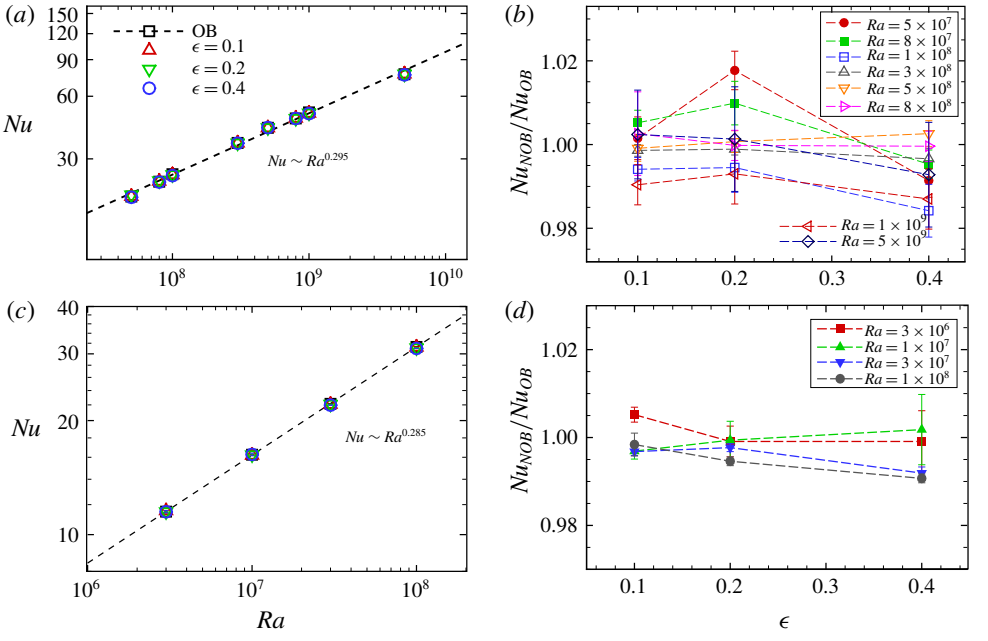

FIGURE 10. The Nusselt number Nu versus Ra for OB and various ϵ for 2-D cases (a) and 3-D cases (c); Nu_{NOB}/Nu_{OB} versus ϵ for various Ra in (b) 2-D cases and (d) 3-D cases. The dashed lines are power-law fitting for OB data.

3.3. *Reynolds numbers*

In RB convection, the Reynolds number Re is an important response parameter, which is defined as

$$Re = \frac{\hat{U}\hat{H}}{\hat{\nu}_0} = \sqrt{\frac{Ra}{Pr}}U, \tag{3.4}$$

where $\hat{U}$ and U are the dimensional and dimensionless characteristic velocities.

Here, we choose the root mean square (r.m.s.) velocities as the characteristic velocity (Wagner & Shishkina 2013; Zhang *et al.* 2017, 2018; Ng *et al.* 2018), i.e. $U = U^{rms} = \sqrt{\langle \boldsymbol{u} \cdot \boldsymbol{u} \rangle_V}$, where $\langle \cdot \rangle_V$ denotes the space average in two and three dimensions and $\boldsymbol{u}$ is the velocity vector. In figure 11(a,c) we show Re based on r.m.s. of velocities as a function of Ra for OB and NOB for various ϵ. Similar to Nu, the Reynolds number can also be expressed by a power-law scaling, i.e. $Re \sim Ra^{\beta}$, as shown in table 2. It is clear that the influence of NOB effects on Re are quite limited, which almost has no influence on the Ra scaling exponents. Based on U^{rms}, the power-law fitting to the data of OB cases yields the scaling of $Re \sim Ra^{0.617}$ in 2-D cases and $Re \sim Ra^{0.491}$ in 3-D cases. For 2-D cases, the scaling exponent 0.617 is in excellent agreement with the exponent 0.62 found for the OB case of water by Sugiyama *et al.* (2009), and is also close to 0.6 reported by Zhang *et al.* (2017) and Wang *et al.* (2019*b*) recently. For 3-D cases, the scaling exponent is notably smaller than that for 2-D RB flows, which agrees with previous findings that this exponent ranges from 0.42 to 0.5 for 3-D RB flows with various working fluids based on one- and multiple-point measurements (Niemela *et al.* 2001; Qiu & Tong 2001; Sun & Xia

Case	OB	$\epsilon = 0.1$	$\epsilon = 0.2$	$\epsilon = 0.4$
2-D	$Re \simeq 0.042Ra^{0.617}$	$Re \simeq 0.044Ra^{0.615}$	$Re \simeq 0.045Ra^{0.613}$	$Re \simeq 0.042Ra^{0.618}$
3-D	$Re \simeq 0.236Ra^{0.491}$	$Re \simeq 0.238Ra^{0.491}$	$Re \simeq 0.235Ra^{0.492}$	$Re \simeq 0.253Ra^{0.487}$

TABLE 2. The best power-law fittings for Re versus Ra for OB and various ϵ in 2-D and 3-D cases.

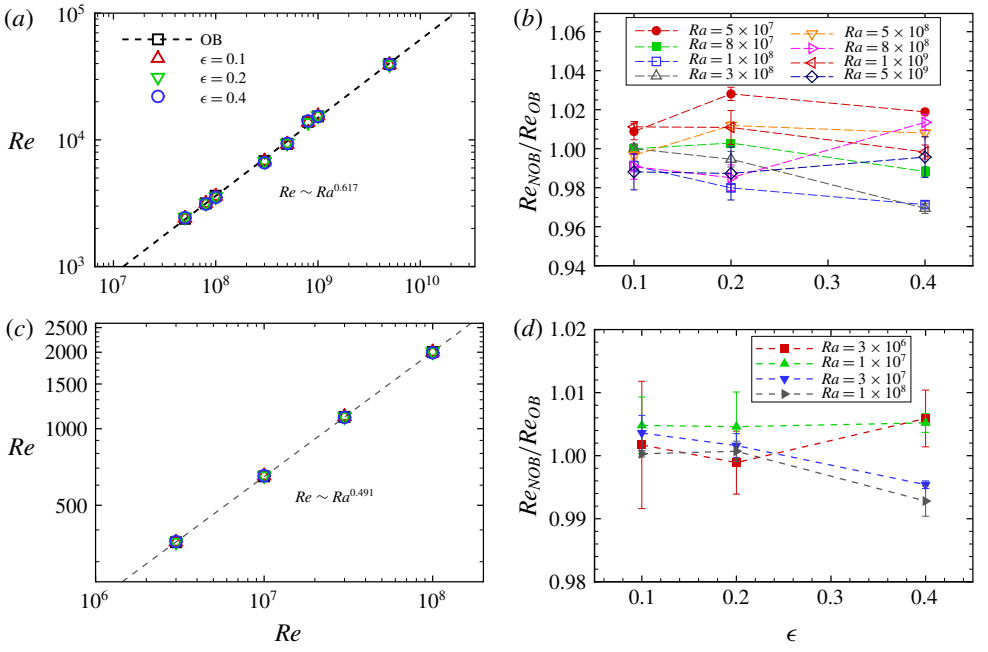

FIGURE 11. The Reynolds number Re^{rms} based on the root mean square (r.m.s.) velocities versus Ra for OB and NOB with various ϵ in (*a*) 2-D and (*c*) 3-D cases. The error bars are smaller than the symbol sizes. The dashed lines are the best power-law fit for OB data. The Reynolds number ratio Re_{NOB}/Re_{OB} versus ϵ at various Ra numbers for (*b*) 2-D and (*d*) 3-D cases.

2005; Brown, Funfschilling & Ahlers 2007). To show the differences quantitatively due to NOB effects, the Reynolds number ratio Re_{NOB}/Re_{OB} versus ϵ for all Ra is presented in figure 11(*b*,*d*). We note that the maximum deviation of Re_{NOB}/Re_{OB} from 1 for all Ra numbers is about 3 % for 2-D cases and about 1 % for 3-D cases. In the scope of the present data, this deviation does not show an obvious growth trend with increasing Ra or ϵ, so we guess that the NOB effects at some higher Ra experiments might also be limited at least for air.

3.4. *The viscous and thermal boundary layers*

The viscous and thermal BLs play an essential role in global heat transport across the fluid layer (Grossmann & Lohse 2000). The Nusselt number is related, directly or intimately, to the thickness of the thermal BLs, due to the fact that within the thermal BLs heat is mainly transported via conduction (Wu & Libchaber 1991; Belmonte,

Tilgner & Libchaber 1994; Lui & Xia 1998). In this section, we are committed to studying the viscous and thermal BLs with strong variations of density, as well as μ and k. The NOB effects on flow structures and heat transport are more significant in 2-D RB flows; thus, we mainly discuss the results for 2-D cases below.

3.4.1. *The extended BL equations for air with a large temperature difference*

Here, we derive the laminar BL equations starting from the non-dimensionalized low-Mach-number Navier–Stokes equations. For derivation of a steady BL solution, we assume time derivatives to be zero ($\partial(\cdot)/\partial t \equiv 0$) in (2.1)–(2.3). Furthermore, we consider a 2-D BL in the x–z plane with a zero-pressure gradient, and the buoyancy term is neglected. The temperature is assumed to be advected passively. Finally, the equations of flow motion are simplified to

$$\frac{\partial \rho u}{\partial x} + \frac{\partial \rho w}{\partial z} = 0, \tag{3.5}$$

$$\rho u \frac{\partial u}{\partial x} + \rho w \frac{\partial u}{\partial z} = \sqrt{\frac{Pr}{Ra}} \frac{\partial}{\partial z}\left(\mu \frac{\partial u}{\partial z}\right), \tag{3.6}$$

$$\rho C_p \left(u \frac{\partial T}{\partial x} + w \frac{\partial T}{\partial z}\right) = \frac{1}{\sqrt{RaPr}} \frac{\partial}{\partial z}\left(k \frac{\partial T}{\partial z}\right). \tag{3.7}$$

Here we further assume that $\rho T = 1$, which is valid for open systems. Furthermore, we introduce a stream function:

$$\rho u = \frac{\partial \Psi}{\partial z}, \quad \rho w = -\frac{\partial \Psi}{\partial x}. \tag{3.8a,b}$$

Next, referring to Ahlers *et al.* (2006, 2007), we further introduce a self-similar variable $\tilde{Z} = z/L$, while $\tilde{\Psi} = \Psi/LU$, such that $L = (Pr/Ra)^{1/4}\sqrt{x/U}$. So the velocity components become

$$u = \frac{U}{\rho}\tilde{\Psi}', \quad w = \sqrt{\frac{Pr}{Ra}} \frac{1}{2\rho L}(\tilde{Z}\tilde{\Psi}' - \tilde{\Psi}). \tag{3.9a,b}$$

Then, the momentum equation becomes

$$\mu\tilde{\Psi}''' + \left(\frac{\tilde{\Psi}}{2} - \mu\frac{2\rho'}{\rho} + \mu'\right)\tilde{\Psi}'' + \left[\mu\left(\frac{2\rho'\rho'}{\rho^2} - \frac{\rho''}{\rho}\right) - \mu'\frac{\rho'}{\rho} - \frac{\tilde{\Psi}}{2}\frac{\rho'}{\rho}\right]\tilde{\Psi}' = 0, \tag{3.10}$$

and the temperature equation becomes

$$kT'' + (k' + \tfrac{1}{2}C_p Pr\tilde{\Psi})T' = 0. \tag{3.11}$$

From the equation of state $\rho = 1/T$, we obtain

$$\mu\tilde{\Psi}''' + \left(\frac{\tilde{\Psi}}{2} + \mu\frac{2T'}{T} + \mu'\right)\tilde{\Psi}'' + \left(\mu\frac{T'''}{T} + \mu'\frac{T'}{T} + \frac{1}{2}\tilde{\Psi}\frac{T'}{T}\right)\tilde{\Psi}' = 0, \tag{3.12}$$

$$kT'' + (k' + \tfrac{1}{2}C_p Pr\tilde{\Psi})T' = 0, \tag{3.13}$$

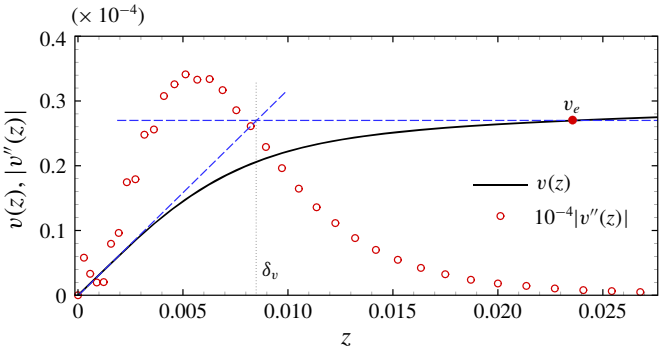

FIGURE 12. The definition of the thickness of viscous BL for DNS results, where the OB case at $Ra = 10^9$ is used. The edge of BL (red dot) with velocity v_e is defined at the position of 3 % of the peak value of the secondary derivative of velocity $|v''(z)|$.

where

$$\mu' = (1 + S_\mu)\left(-\frac{T^{1.5}}{(T + S_\mu)^2} + \frac{1.5T^{0.5}}{(T + S_\mu)}\right)T', \tag{3.14}$$

$$k' = (1 + S_k)\left(-\frac{T^{1.5}}{(T + S_k)^2} + \frac{1.5T^{0.5}}{(T + S_k)}\right)T', \tag{3.15}$$

and the boundary conditions

$$\Psi(0) = 0, \quad \Psi'(0) = 0, \quad \Psi'(\infty) = \rho_\infty, \tag{3.16a–c}$$

$$T(0) = T_w, \quad T(\infty) = T_\infty. \tag{3.17a,b}$$

In this paper, we use the density and temperature at the cell centre from DNS results to define the boundary conditions for the BL equations at infinity (ρ_∞, T_∞). Here, T_w is the temperature at the wall as sketched in figure 1, i.e. $T_w = 1 + \epsilon$ (hot plate) or $T_w = 1 - \epsilon$ (cold plate). Then, the new BL equations can be solved by the shooting method, the results of which are compared to the DNS results in § 3.4.2.

3.4.2. *The viscous/thermal boundary layer*

Here, in some cases, we cannot find the maximum velocity near the BL edge as shown in figure 3(*b*). Therefore, we use a new definition of the thickness of the viscous BL (δ_v) as illustrated in figure 12, which is slightly different from that in prior studies (Sun, Cheung & Xia 2008; Wei & Xia 2013). According to BL theory, the viscous effects mainly come from the term containing the secondary derivative of velocity. In order to find the edge of the viscous BL, we calculate the secondary derivative of velocity with respect to z, i.e. $v''(z)$, and set the location of 3 % of the peak value of $|v''(z)|$ to be the edge of the viscous BL, ensuring that the viscous effects become small at this location and beyond. Then, the velocity at the edge of the viscous BL is denoted as v_e. The thickness of the viscous BL δ_v is defined as the distance from the wall at which the extrapolation of the linear part of the horizontal velocity profile meets the horizontal line passing through the velocity v_e. We examined that, for $Ra = 10^8$, this difference of δ_v between current and prior definitions is less

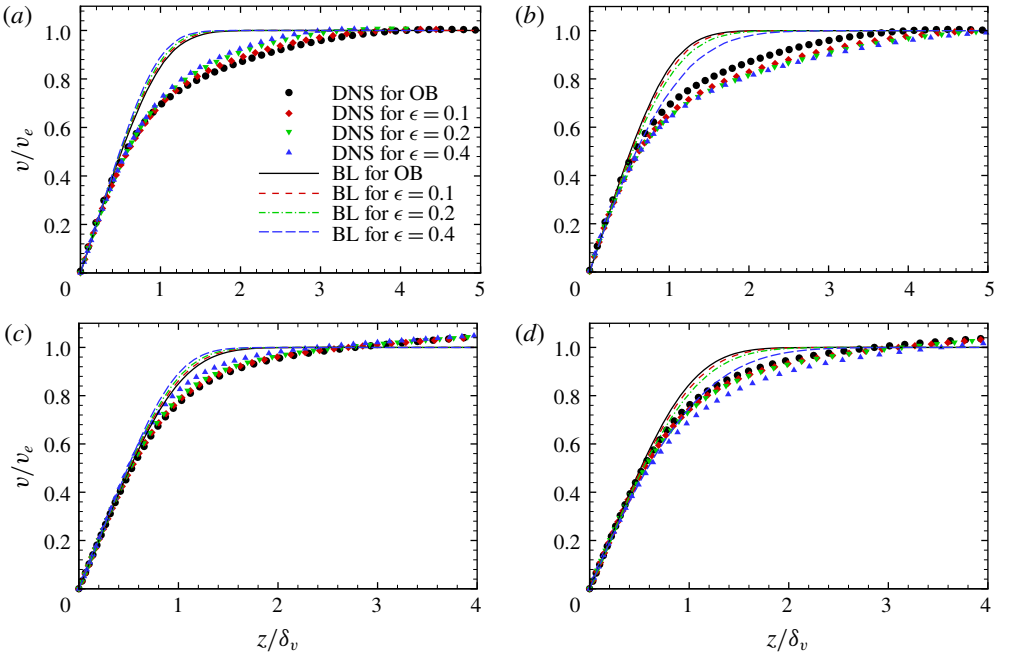

FIGURE 13. The comparison of normalized velocity profiles of current BL equations and DNS results for OB and NOB cases with different Ra on the line $y = 0.5$. (*a*,*b*) $Ra = 10^8$, (*c*,*d*) $Ra = 10^9$. (*a*,*c*) The BL profiles on the bottom plate. (*b*,*d*) The BL profiles on the top plate. Here, δ_v is the thickness of the viscous BL and u_e is the velocity at the edge of the BL.

than 1 %. The thickness of the thermal BL (δ_T) can also be defined using the centre temperature T_c in a similar way (Zhou & Xia 2013).

In figure 13 we show the profiles of normalized velocity $v(z)/v_e$ as a function of z/δ_v for $Ra = 10^8$, 10^9 for OB and NOB cases on the line $y = 0.5$ in 2-D cases. For each DNS case, the combination of v_e and δ_v can be uniquely determined. Due to symmetry breaking under NOB conditions, the velocity profile on the bottom (top, respectively) plate is shown in figure 13(*a*,*c*) (figure 13*b*,*d*, respectively). There are some deviations of the velocity profile between the solutions of the present BL equations and DNS which are also found in experiments by (Wei & Xia 2013), and DNS by (Shi, Emran & Schumacher 2012). However, we find a similar trend of viscous BL profiles due to NOB effects between the extended BL solutions and DNS. Clearly, we find that the changes of the normalized velocity profiles on the bottom plate and the top plate are opposite. The deviations could result from the generation of plumes, pressure gradient and time variation of the BL, since the laminar BL theory relies on a series of assumptions. However, in general, our extended BL equations can reasonably predict the influence of NOB effects on the velocity profiles, regardless of the Ra. In figure 14 we further show the profiles of Θ as a function of z/δ_T for $Ra = 10^8$, 10^9 for both OB and NOB cases. The value of δ_T for each DNS case is determined according to δ_v, since equations (3.10) and (3.11) are coupled. Again, the temperature profiles obtained by extended BL equations agree qualitatively with the DNS results, and we still observe a certain degree of deviations near the edge of thermal BLs.

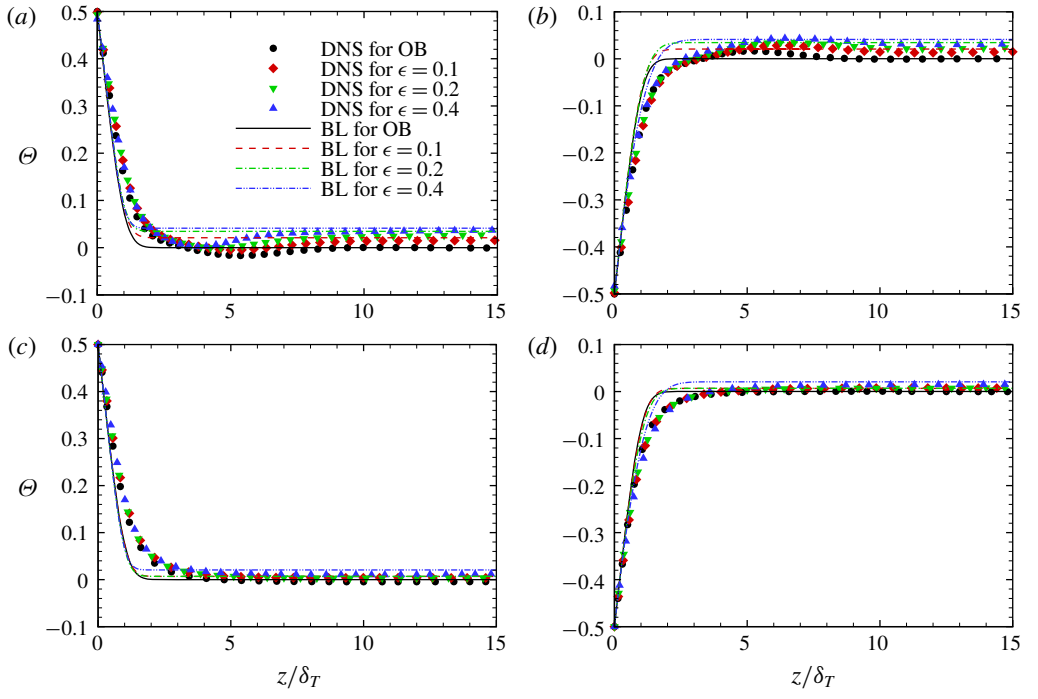

FIGURE 14. The comparison of normalized temperature profiles of BL theory and DNS results as a function of z/δ_T for OB and NOB cases with different Ra. (*a*,*b*) $Ra = 10^8$, (*c*,*d*) $Ra = 10^9$. (*a*,*c*) The temperature profiles on the bottom plate. (*b*,*d*) The temperature profiles on the top plate. δ_T is the thickness of thermal BL.

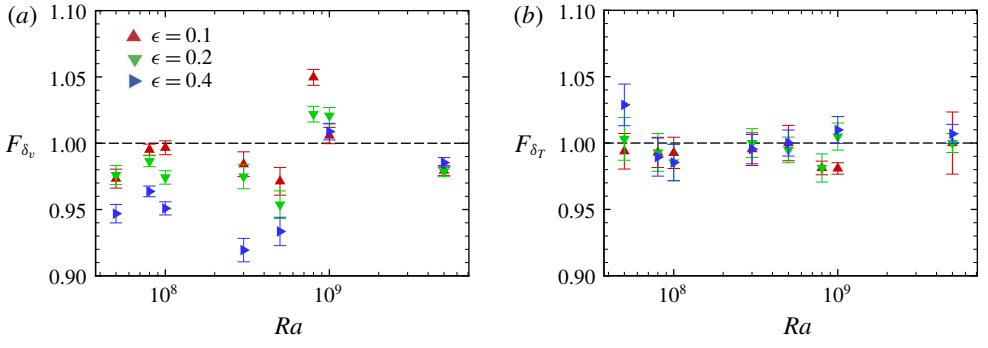

FIGURE 15. The compensation of viscous and thermal BLs. (*a*) F_{δ_v} and (*b*) F_{δ_T} versus Ra for various ϵ for 2-D cases on the line at $y = 0.5$.

As shown in figure 13, we easily find that the thickness of the viscous/thermal BL is increased near the hot plate due to NOB effects, and decreased near the cold plate. In figure 15 we compare the sum of thicknesses of the top and bottom viscous/thermal BL for the NOB case to the OB case by calculating the ratios F_{δ_v} and F_{δ_T} at $y = 0.5$

for 2-D cases, which are defined as

$$F_{\delta_v} = 2\delta_v^{OB}/(\delta_v^t + \delta_v^b)^{NOB}; \quad F_{\delta_T} = 2\delta_T^{OB}/(\delta_T^t + \delta_T^b)^{NOB}. \tag{3.18a,b}$$

From figure 15(*a*), it can be seen that there are relatively strong deviations from 1 for F_{δ_v} (at most around 6 %), which are also *Ra*-dependent. For $Ra \lesssim 8 \times 10^8$, the NOB effects on velocity fields are relatively stronger. For higher *Ra*, the LSC is broken, the corner rolls become unstable and the velocity fields are dominated by smaller vortex structures, which weaken the impact of NOB effects. In contrast to F_{δ_v}, the NOB effects have less impact on F_{δ_T}. The maximum deviation from 1 for F_{δ_T} is at most around 3 % due to cancellations between δ_T^t and δ_T^b, close to the deviations of Nu_{NOB}/Nu_{OB}, but no tendency can be seen. In water under NOB conditions, Ahlers *et al.* (2006) also attributed the robustness of *Nu* towards NOB effects to a compensation effect of top and bottom thermal BLs. Present data for air – even with large temperature differences – seem to support this statement, suggesting that this mechanism holds in different systems under NOB conditions. As previously mentioned, the flow structure is reorganized around $Ra \simeq 8 \times 10^8$ in 2-D cases, but one cannot observe any clear transition from the data of F_{δ_T}.

4. Summary and conclusions

To summarize, we have systematically studied 2-D and 3-D RB convection of air under NOB conditions due to large temperature differences by DNS. We consider the turbulence system with large temperature differences (60 K–240 K), which gives rise in large density variations. The extremely large temperature difference case with $\Delta\hat{T} = 240$ K is also considered, which has not been reached in previous experiments. The strong NOB effects are induced in a moderate *Ra* range $3 \times 10^6 \leqslant Ra \leqslant 5 \times 10^9$. To the best of our knowledge, the low-Mach-number Navier–Stokes equations are firstly employed in order to treat 3-D turbulence with large density variations and temperature-dependent fluid properties in RB convection at relatively high *Ra* (Livescu 2020).

Firstly, for air with large density variations, the top-down symmetry is broken with NOB effects which induces some changes in flow organizations, such as the shift of centre temperature T_c and the asymmetry of the velocity/thermal BLs. The T_c is increased under NOB conditions compared to the arithmetic mean temperature of the top and bottom plates T_m, which is different from ethane gas close to its critical point (Ahlers *et al.* 2007). The maximum relative deviation $(T_c - T_m)/2\epsilon$ is around 5 % in 2-D cases, while it becomes quite small in 3-D cases. As reported by Ahlers *et al.* (2006) and Sugiyama *et al.* (2009), the T_c for water under NOB conditions are weakly dependent on *Ra*, which can be generally predicted by an extended Prandtl–Blasius theory. However, this theory fails in the present system due to the fact that present results of T_c are scattered and strongly dependent on *Ra*. Combined with previous experimental and numerical results, we can conclude that the deviation of the centre temperature is sensitively dependent on the particular working fluid.

Moreover, for all *Ra* and ϵ explored, we find that the NOB effects have a very limited influence on *Nu*. The Nusselt number Nu_{NOB} will differ from Nu_{OB} by 2 % or less regardless of the existence of stable LSC. The Nusselt number ratios Nu_{NOB}/Nu_{OB} are *Ra*- and ϵ-dependent, while they are only weakly dependent on *Ra* for water with NOB effects (Sugiyama *et al.* 2009; Demou & Grigoriadis 2019). More importantly, we also find that the power-law scaling of $Nu \sim Ra^{\alpha}$ is rather insensitive to the

NOB effects. The maximum influence of NOB effects on *Re* is around 3 % for 2-D cases and 1 % for 3-D cases, which are also *Ra*- and ϵ-dependent. In general, the NOB effects on *Nu* and *Re* are much weaker in 3-D cases. This finding is also different from that for low-temperature gaseous helium (Sameen *et al.* 2008) in a 3-D cylindrical cell. Besides, unlike the NOB effects in water, the extremely large temperature differences induce large density variations, which is the most significant feature of the present system; however, the effects of large density variations seem to play a very limited role on global heat and momentum transport in the scope of the present study.

Finally, the extended BL equations based on low-Mach-number Navier–Stokes equations are developed, involving the strong variation of density, as well as the temperature-dependent fluid properties. The NOB effects on BL velocity profiles shown by DNS are predicted qualitatively by the extended BL theory in spite of the large deviations in the z dependence of horizontal mean velocity profiles on the line $y = 0.5$ for 2-D cases. With increasing ϵ, the relative velocity inside BLs near the hot plate is increased, while it decreases near the cold plate. From F_{δ_v} and F_{δ_T} data, we interestingly find that the NOB effects have a much stronger impact on the viscous BLs than the thermal BLs. For all *Ra* explored, the F_{δ_T} data are scattered but their deviations from 1 are at most around 3 %, close to the deviations of Nu_{NOB}/Nu_{OB}. In the present system, the data also supports the fact that the compensation effect between the top and bottom thermal BL leads to the robustness of *Nu* against the NOB effects, suggesting that this mechanism holds in many different systems under NOB conditions.

In a word, this study fills the gap of numerical study of NOB effects in air with large temperature differences at relatively high *Ra* in both 2-D and 3-D systems. The results show that the power-law scalings for *Nu* and *Re* versus *Ra* are rather insensitive to the NOB effects for air, in particular for 3-D RB flows, which implies that the NOB effects may play a very limited role for *Nu* and *Re* at some high *Ra* experiments with large temperature differences in air or other perfect gases.

Acknowledgements

This work is supported by the National Natural Science Foundation of China (NSFC) under grants 91952103, 11821202, 11825204 and 11621202, and the Fundamental Research Funds for the Central Universities. S.-N.X. thanks the fund of China Postdoctoral Science Foundation (2016M600306) and the NSFC under grant 11702167.

Declaration of interests

The authors report no conflict of interest.

Supplementary movies

Supplementary movies are available at https://doi.org/10.1017/jfm.2020.66.

Appendix. Details of the simulation parameters

The detailed simulation parameters and results are presented in tables 3 and 4.

Case	Ra	$N_x \times N_z$	t_{avg}	N_{BL}^b	N_{BL}^t	Nu	Nu_V	Re
OB	5×10^7	256×256	1500	14	14	19.77 ± 0.06	19.71	2385 ± 6
$\epsilon = 0.1$		384×384	1500	20	22	19.80 ± 0.10	—	2406 ± 10
$\epsilon = 0.2$		384×384	1500	19	23	20.12 ± 0.09	—	2452 ± 8
$\epsilon = 0.4$		384×384	1500	16	26	19.60 ± 0.08	—	2430 ± 3
OB	8×10^7	384×384	1500	18	18	23.30 ± 0.09	23.28	3153 ± 7
$\epsilon = 0.1$		512×512	1500	30	33	23.42 ± 0.07	—	3153 ± 4
$\epsilon = 0.2$		512×512	1500	28	34	23.53 ± 0.12	—	3162 ± 5
$\epsilon = 0.4$		512×512	1500	23	37	23.19 ± 0.08	—	3116 ± 8
OB	1×10^8	384×384	1000	17	17	25.31 ± 0.10	25.21	3623 ± 8
$\epsilon = 0.1$		512×512	1000	28	30	25.16 ± 0.07	—	3591 ± 9
$\epsilon = 0.2$		512×512	1000	26	32	25.17 ± 0.15	—	3550 ± 6
$\epsilon = 0.4$		512×512	1000	22	35	24.91 ± 0.16	—	3519 ± 6
OB	3×10^8	512×512	1000	17	17	35.79 ± 0.12	35.63	6793 ± 8
$\epsilon = 0.1$		512×512	1000	21	22	35.74 ± 0.05	—	6805 ± 17
$\epsilon = 0.2$		512×512	1200	20	23	35.75 ± 0.05	—	6768 ± 27
$\epsilon = 0.4$		512×512	1600	17	25	35.67 ± 0.09	—	6597 ± 18
OB	5×10^8	512×512	1000	14	14	42.32 ± 0.07	42.26	9298 ± 25
$\epsilon = 0.1$		512×512	1000	14	19	42.28 ± 0.13	—	9266 ± 17
$\epsilon = 0.2$		512×512	1000	13	20	42.35 ± 0.11	—	9409 ±17
$\epsilon = 0.4$		512×512	1600	11	22	42.43 ± 0.13	—	9372 ± 16
OB	8×10^8	768×768	800	20	20	46.94 ± 0.45	47.31	13896 ± 47
$\epsilon = 0.1$		768×768	800	19	21	47.06 ± 0.47	—	13768 ± 91
$\epsilon = 0.2$		768×768	1000	16	22	46.93 ± 0.17	—	13689 ± 92
$\epsilon = 0.4$		768×768	900	14	22	46.92 ± 0.17	—	14084 ± 59
OB	1×10^9	768×768	800	21	21	50.18 ± 0.25	50.01	15327 ± 123
$\epsilon = 0.1$		768×768	800	20	22	49.70 ± 0.24	—	15499 ± 41
$\epsilon = 0.2$		768×768	1000	19	23	49.83 ± 0.36	—	15494 ± 134
$\epsilon = 0.4$		768×768	800	17	24	49.53 ± 0.36	—	15301 ± 55
OB	5×10^9	1152×1152	600	21	21	76.58 ± 0.63	76.49	39691 ± 520
$\epsilon = 0.1$		1152×1152	800	20	21	76.76 ± 0.81	—	39218 ± 365
$\epsilon = 0.2$		1152×1152	1000	19	22	76.68 ± 0.96	—	39187 ± 538
$\epsilon = 0.4$		1152×1152	800	17	23	76.03 ± 0.96	—	39520 ± 412

TABLE 3. Simulation parameters for 2-D cases. The columns from left to right indicate the following: OB and various ϵ cases (NOB); Rayleigh number Ra; grid size ($N_x \times N_z$); the averaging time for calculating statistics t_{avg}; the number of grid points within the bottom thermal BL N_{BL}^b; the number of grid points within the top thermal BL N_{BL}^t; Nusselt numbers Nu measured at the bottom plate; Nusselt numbers $Nu_V = \sqrt{RaPr}\langle\epsilon_u\rangle_{V,t} + 1$ measured by the globally averaged kinetic energy dissipation rates; and Reynolds numbers $Re = \sqrt{Ra/Pr}U^{rms}$. The Prandtl number Pr is fixed to 0.71.

Case	Ra	$N_x \times N_y \times N_z$	t_{avg}	N_{BL}^b	N_{BL}^t	Nu	Nu_V	Re
OB	3×10^6	$128 \times 128 \times 128$	500	13	13	11.50 ± 0.08	11.47	357.8 ± 2.7
$\epsilon = 0.1$		$128 \times 128 \times 128$	500	12	12	11.56 ± 0.02	—	358.4 ± 3.6
$\epsilon = 0.2$		$128 \times 128 \times 128$	500	12	11	11.49 ± 0.04	—	357.4 ± 1.8
$\epsilon = 0.4$		$128 \times 128 \times 128$	500	11	10	11.49 ± 0.08	—	359.9 ± 1.6
OB	1×10^7	$192 \times 192 \times 192$	400	19	19	16.25 ± 0.05	16.23	649.6 ± 2.5
$\epsilon = 0.1$		$192 \times 192 \times 192$	400	20	18	16.20 ± 0.03	—	652.7 ± 2.9
$\epsilon = 0.2$		$192 \times 192 \times 192$	400	21	17	16.24 ± 0.07	—	652.6 ± 3.6
$\epsilon = 0.4$		$192 \times 192 \times 192$	400	22	15	16.28 ± 0.13	—	653.0 ± 1.0
OB	3×10^7	$256 \times 256 \times 288$	400	21	21	22.14 ± 0.04	22.15	1112.9 ± 1.5
$\epsilon = 0.1$		$256 \times 256 \times 288$	400	22	20	22.07 ± 0.02	—	1116.9 ± 3.1
$\epsilon = 0.2$		$256 \times 256 \times 288$	400	23	19	22.09 ± 0.02	—	1114.7 ± 2.1
$\epsilon = 0.4$		$256 \times 256 \times 288$	400	25	17	21.96 ± 0.03	—	1107.8 ± 0.7
OB	1×10^8	$384 \times 384 \times 392$	400	28	28	31.29 ± 0.02	31.39	2004.1 ± 4.6
$\epsilon = 0.1$		$384 \times 384 \times 392$	400	29	26	31.24 ± 0.08	—	2004.7 ± 1.1
$\epsilon = 0.2$		$384 \times 384 \times 392$	400	31	25	31.12 ± 0.03	—	2005.6 ± 3.3
$\epsilon = 0.4$		$384 \times 384 \times 392$	400	33	22	31.00 ± 0.03	—	1989.6 ± 4.9

TABLE 4. Simulation parameters for 3-D cases. The columns from left to right indicate the following: OB and various ϵ cases (NOB); Rayleigh number Ra; grid size ($N_x \times N_y \times N_z$); the averaging time for calculating statistics t_{avg}; the number of grid points within the bottom thermal BL N_{BL}^b; the number of grid points within the top thermal BL N_{BL}^t; Nusselt numbers Nu measured at the bottom plate; Nusselt numbers $Nu_V = \sqrt{RaPr}\langle\epsilon_u\rangle_{V,t} + 1$ measured by the globally averaged kinetic energy dissipation rates; and Reynolds numbers $Re = \sqrt{Ra/Pr}U^{rms}$. The Prandtl number Pr is fixed to 0.71.

REFERENCES

AHLERS, G., ARAUJO, F. F., FUNFSCHILLING, D., GROSSMANN, S. & LOHSE, D. 2007 Non-Oberbeck–Boussinesq effects in gaseous Rayleigh–Bénard convection. *Phys. Rev. Lett.* **98** (5), 054501.

AHLERS, G., BROWN, E., ARAUJO, F. F., FUNFSCHILLING, D., GROSSMANN, S. & LOHSE, D. 2006 Non-Oberbeck–Boussinesq effects in strongly turbulent Rayleigh–Bénard convection. *J. Fluid Mech.* **569**, 409–445.

AHLERS, G., CALZAVARINI, E., ARAUJO, F. F., FUNFSCHILLING, D., GROSSMANN, S., LOHSE, D. & SUGIYAMA, K. 2008 Non-Oberbeck–Boussinesq effects in turbulent thermal convection in ethane close to the critical point. *Phys. Rev.* E **77** (4), 046302.

AHLERS, G., GROSSMANN, S. & LOHSE, D. 2009 Heat transfer and large scale dynamics in turbulent Rayleigh–Bénard convection. *Rev. Mod. Phys.* **81** (2), 503–537.

BELMONTE, A., TILGNER, A. & LIBCHABER, A. 1994 Temperature and velocity boundary layers in turbulent convection. *Phys. Rev.* E **50** (1), 269.

BODENSCHATZ, E., PESCH, W. & AHLERS, G. 2000 Recent developments in Rayleigh–Bénard convection. *Annu. Rev. Fluid Mech.* **32** (1), 709–778.

BRIGGS, W. L., HENSON, V. E. & MCCORMICK, S. F. 2000 *A Multigrid Tutorial*, vol. 72. SIAM.

BROWN, E., FUNFSCHILLING, D. & AHLERS, G. 2007 Anomalous Reynolds-number scaling in turbulent Rayleigh–Bénard convection. *J. Stat. Mech.* **2007** (10), P10005.

BURNISHEV, Y., SEGRE, E. & STEINBERG, V. 2010 Strong symmetrical non-Oberbeck–Boussinesq turbulent convection and the role of compressibility. *Phys. Fluids* **22** (3), 035108.

BURNISHEV, Y. & STEINBERG, V. 2012 Statistics and scaling properties of temperature field in symmetrical non-Oberbeck–Boussinesq turbulent convection. *Phys. Fluids* **24** (4), 045102.

CHANDRA, M. & VERMA, M. K. 2013 Flow reversals in turbulent convection via vortex reconnections. *Phys. Rev. Lett.* **110** (11), 114503.

CHEN, L.-W., XU, C.-Y. & LU, X.-Y. 2010 Numerical investigation of the compressible flow past an aerofoil. *J. Fluid Mech.* **643**, 97–126.

CHILLÀ, F. & SCHUMACHER, J. 2012 New perspectives in turbulent Rayleigh–Bénard convection. *Eur. Phys. J.* E **35** (7), 1–25.

DEMOU, A. D. & GRIGORIADIS, D. G. E. 2019 Direct numerical simulations of Rayleigh–Bénard convection in water with non-Oberbeck–Boussinesq effects. *J. Fluid Mech.* **881**, 1073–1096.

GRAY, D. D. & GIORGINI, A. 1976 The validity of the Boussinesq approximation for liquids and gases. *Intl J. Heat Mass Transfer* **19** (5), 545–551.

GROSSMANN, S. & LOHSE, D. 2000 Scaling in thermal convection: a unifying theory. *J. Fluid Mech.* **407**, 27–56.

HORN, S. & SHISHKINA, O. 2014 Rotating non-Oberbeck–Boussinesq Rayleigh–Bénard convection in water. *Phys. Fluids* **26** (5), 055111.

HORN, S., SHISHKINA, O. & WAGNER, C. 2013 On non-Oberbeck–Boussinesq effects in three-dimensional Rayleigh–Bénard convection in glycerol. *J. Fluid Mech.* **724**, 175–202.

JOHNSTON, H. & DOERING, C. R. 2009 Comparison of turbulent thermal convection between conditions of constant temperature and constant flux. *Phys. Rev. Lett.* **102** (6), 064501.

LIU, S., XIA, S.-N., YAN, R., WAN, Z.-H. & SUN, D.-J. 2018 Linear and weakly nonlinear analysis of Rayleigh–Bénard convection of perfect gas with non-Oberbeck–Boussinesq effects. *J. Fluid Mech.* **845**, 141–169.

LIVESCU, D. 2020 Turbulence with large thermal and compositional density variations. *Annu. Rev. Fluid Mech.* **52**, 309–341.

LOHSE, D. & XIA, K.-Q. 2010 Small-scale properties of turbulent Rayleigh–Bénard convection. *Annu. Rev. Fluid Mech.* **42**, 335–364.

LUI, S.-L. & XIA, K.-Q. 1998 Spatial structure of the thermal boundary layer in turbulent convection. *Phys. Rev.* E **57** (5), 5494.

NG, C. S., OOI, A., LOHSE, D. & CHUNG, D. 2018 Bulk scaling in wall-bounded and homogeneous vertical natural convection. *J. Fluid Mech.* **841**, 825–850.

NIEMELA, J. J., SKRBEK, L., SREENIVASAN, K. R. & DONNELLY, R. J. 2001 The wind in confined thermal convection. *J. Fluid Mech.* **449**, 169–178.

PAOLUCCI, S. 1982 Filtering of sound from the Navier–Stokes equations. NASA STI *Tech. Rep.* Recon Tech. Rep. N, 83, 26036.

PIROZZOLI, S., BERNARDINI, M. & GRASSO, F. 2010 Direct numerical simulation of transonic shock/boundary layer interaction under conditions of incipient separation. *J. Fluid Mech.* **657**, 361–393.

VAN DER POEL, E. P., OSTILLA-MNICO, R., DONNERS, J. & VERZICCO, R. 2015 A pencil distributed finite difference code for strongly turbulent wall-bounded flows. *Comput. Fluids* **116**, 10–16.

VAN DER POEL, E. P., STEVENS, R. J. A. M., SUGIYAMA, K. & LOHSE, D. 2012 Flow states in two-dimensional Rayleigh–Bénard convection as a function of aspect-ratio and Rayleigh number. *Phys. Fluids* **24** (8), 085104.

QIU, X.-L. & TONG, P. 2001 Large-scale velocity structures in turbulent thermal convection. *Phys. Rev.* E **64** (3), 036304.

SAMEEN, A., VERZICCO, R. & SREENIVASAN, K. R. 2008 Non-Boussinesq convection at moderate Rayleigh numbers in low temperature gaseous helium. *Phys. Scr.* **2008** (T132), 014053.

SAMEEN, A., VERZICCO, R. & SREENIVASAN, K. R. 2009 Specific roles of fluid properties in non-Boussinesq thermal convection at the Rayleigh number of 2×10^8. *Eur. Phys. Lett.* **86** (1), 14006.

SHI, N., EMRAN, M. S. & SCHUMACHER, J. 2012 Boundary layer structure in turbulent Rayleigh–Bénard convection. *J. Fluid Mech.* **706**, 5–33.

SHISHKINA, O., STEVENS, R. J. A. M., GROSSMANN, S. & LOHSE, D. 2010 Boundary layer structure in turbulent thermal convection and its consequences for the required numerical resolution. *New J. Phys.* **12** (7), 075022.

SUGIYAMA, K., CALZAVARINI, E., GROSSMANN, S. & LOHSE, D. 2007 Non-Oberbeck–Boussinesq effects in two-dimensional Rayleigh–Bénard convection in glycerol. *Eur. Phys. Lett.* **80** (3), 34002.

SUGIYAMA, K., CALZAVARINI, E., GROSSMANN, S. & LOHSE, D. 2009 Flow organization in two-dimensional non-Oberbeck–Boussinesq Rayleigh–Bénard convection in water. *J. Fluid Mech.* **637**, 105–135.

SUN, C., CHEUNG, Y.-H. & XIA, K.-Q. 2008 Experimental studies of the viscous boundary layer properties in turbulent Rayleigh–Bénard convection. *J. Fluid Mech.* **605**, 79–113.

SUN, C. & XIA, K.-Q. 2005 Scaling of the Reynolds number in turbulent thermal convection. *Phys. Rev.* E **72** (6), 067302.

SUSLOV, S. A. 2010 Mechanism of nonlinear flow pattern selection in moderately non-Boussinesq mixed convection. *Phys. Rev.* E **81** (2), 026301.

SUSLOV, S. A. & PAOLUCCI, S. 1999 Nonlinear stability of mixed convection flow under non-Boussinesq conditions. Part 1. Analysis and bifurcations. *J. Fluid Mech.* **398**, 61–85.

SUTHERLAND, W. 1893 The viscosity of gases and molecular force. *Lond. Edinb. Dublin Phil. Mag. J. Sci.* **36**, 507–531.

VALORI, V., ELSINGA, G., ROHDE, M., TUMMERS, M., WESTERWEEL, J. & VAN DER HAGEN, T. 2017 Experimental velocity study of non-Boussinesq Rayleigh–Bénard convection. *Phys. Rev.* E **95** (5), 053113.

VERZICCO, R. & ORLANDI, P. 1996 A finite-difference scheme for three-dimensional incompressible flows in cylindrical coordinates. *J. Comput. Phys.* **123** (2), 402–414.

WAGNER, S. & SHISHKINA, O. 2013 Aspect-ratio dependency of Rayleigh–Bénard convection in box-shaped containers. *Phys. Fluids* **25** (8), 085110.

WAN, Z.-H., ZHOU, L., YANG, H.-H. & SUN, D.-J. 2013 Large eddy simulation of flow development and noise generation of free and swirling jets. *Phys. Fluids* **25** (12), 126103.

WANG, Q., XIA, S.-N., WANG, B.-F., SUN, D.-J., ZHOU, Q. & WAN, Z.-H. 2018 Flow reversals in two-dimensional thermal convection in tilted cells. *J. Fluid Mech.* **849**, 355–372.

WANG, Q., XIA, S.-N., YAN, R., SUN, D.-J. & WAN, Z.-H. 2019*a* Non-Oberbeck-Boussinesq effects due to large temperature differences in a differentially heated square cavity filled with air. *Intl J. Heat Mass Transfer* **128**, 479–491.

WANG, Q., ZHOU, Q., WAN, Z.-H. & SUN, D.-J. 2019*b* Penetrative turbulent Rayleigh–Bénard convection in two and three dimensions. *J. Fluid Mech.* **870**, 718–734.

WEI, P. & XIA, K.-Q. 2013 Viscous boundary layer properties in turbulent thermal convection in a cylindrical cell: the effect of cell tilting. *J. Fluid Mech.* **720**, 140–168.

WEISS, S., HE, X., AHLERS, G., BODENSCHATZ, E. & SHISHKINA, O. 2018 Bulk temperature and heat transport in turbulent Rayleigh–Bénard convection of fluids with temperature-dependent properties. *J. Fluid Mech.* **851**, 374–390.

WHITE, F. M. 1974 *Viscous Fluid Flow*. McGraw-Hill.

WU, X.-Z. & LIBCHABER, A. 1991 Non-Boussinesq effects in free thermal convection. **43** (6), 2833–2839.

XI, H.-D., LAM, S. & XIA, K.-Q. 2004 From laminar plumes to organized flows: the onset of large-scale circulation in turbulent thermal convection. *J. Fluid Mech.* **503**, 47–56.

XIA, K.-Q. 2013 Current trends and future directions in turbulent thermal convection. *Theor. Appl. Mech. Lett.* **05**, 3–14.

XIA, S.-N., WAN, Z.-H., LIU, S., WANG, Q. & SUN, D.-J. 2016 Flow reversals in Rayleigh–Bénard convection with non-Oberbeck–Boussinesq effects. *J. Fluid Mech.* **798**, 628–642.

ZHANG, J., CHILDRESS, S. & LIBCHABER, A. 1997 Non-Boussinesq effect: thermal convection with broken symmetry. *Phys. Fluids* **9** (4), 1034–1042.

ZHANG, J., CHILDRESS, S. & LIBCHABER, A. 1998 Non-Boussinesq effect: asymmetric velocity profiles in thermal convection. *Phys. Fluids* **10** (6), 1534–1536.

ZHANG, Y., ZHOU, Q. & SUN, C. 2017 Statistics of kinetic and thermal energy dissipation rates in two-dimensional turbulent Rayleigh–Bénard convection. *J. Fluid Mech.* **814**, 165–184.

ZHANG, Y.-Z., SUN, C., BAO, Y. & ZHOU, Q. 2018 How surface roughness reduces heat transport for small roughness heights in turbulent Rayleigh–Bénard convection. *J. Fluid Mech.* **836**, R2.

ZHOU, Q. & XIA, K.-Q. 2013 Thermal boundary layer structure in turbulent Rayleigh–Bénard convection in a rectangular cell. *J. Fluid Mech.* **721**, 199–224.